

Coupled shell-material point method for bird strike simulation[☆]

Bo Wu^a, Zhenpeng Chen^a, Xiong Zhang^{a,*}, Yan Liu^a, Yanping Lian^{a,b}

^a*School of Aerospace Engineering, Tsinghua University, Beijing 100084, China*

^b*Department of Mechanical Engineering, Northwestern University, Evanston, IL 60208, USA*

Abstract

In a bird strike, the bird undergoes large deformation like flows; while most part of the structure is in small deformation, the region near the impact point may experience large deformations, even fail. This paper develops a coupled shell-material point method (CSMPM) for bird strike simulation, in which the bird is modeled by the material point method (MPM) and the aircraft structure is modeled by the Belytschko-Lin-Tsay shell element. The interaction between the bird and the structure is handled by a particle-to-surface contact algorithm. The distorted and failed shell elements will be eroded if a certain criterion is reached. The proposed CSMPM takes full advantages of both the finite element method (FEM) and the material point method (MPM) for bird strike simulation, and is validated by several numerical examples.

Keywords: bird strike simulation, material point method, shell element, coupling, adaptive conversion

1. Introduction

Bird strike is one of the most important safety concerns in aviation industries^[1–3]. In the year 2014, about 13,000 bird strikes were reported to the Federal Aviation Administration (FAA)^[4]. Consequently, specific aviation regulations have been laid out, requiring aircraft to be certified for a proven level of bird impact resistance before coming into service.

A bird strike happens with high intensity and short duration. At the velocities of interest, the stresses of the bird are significantly higher than its own strength, so the bird behaves as a soft body and undergoes large deformations like flows over the structure^[3,5]. In addition, a deep interaction exists between the impact loads and the dynamic response of structure. Therefore, it is hard to model the bird strike accurately.

Before powerful computers came out, only theoretical and experimental approaches were used for the study of bird strike. Wilbeck and Barber^[5] studied the bird strike on a flat rigid plate using the hydrodynamic theory of soft body impacts, and their results showed good accordance with the experimental data. However, the theoretical approach can be hardly used in practical applications, because it introduces too many approximations and simplified assumptions^[3].

On the other hand, experiment is the most reliable method to prove the bird impact resistance of structures. Many researchers have conducted specific experimental tests, but their results are usually not available to the public. Besides, a bird strike experiment is difficult to be carried out, because it is expensive and time consuming. Especially, a bird-strike test requires costly testing equipment, very accurate measurement devices, and an intact aircraft component, which is very expensive but useless after being damaged in the tests^[3].

Numerical methods for developing high-efficiency bird-proof structures^[6] have become popular. The finite element method (FEM) has been successfully used to model aircraft structures. In a bird strike simulation, the major challenge is to simulate the highly-deformed bird. Several numerical approaches have been established to discretize the bird, including the FEM, arbitrary Lagrangian-Eulerian (ALE) method, and Smoothed Particle Hydrodynamics (SPH)^[1,3]. However, none of them is free from disadvantages: FEM encounters mesh distortion; ALE is complex in material interface capturing and convection calculating; and SPH is

[☆]Supported by the National Natural Science Foundation of China (11390363).

*Corresponding author

Email address: xzhang@tsinghua.edu.cn (Xiong Zhang)

somewhat time consuming due to neighbor searching^[1,3,7] and suffers from boundary deficiency and tensile instability. In general, SPH is preferred by most researchers^[7,8].

Like SPH, material point method (MPM)^[9,10] is also a particle method. In the MPM, the material domain is discretized by a set of Lagrangian material points (particles), which carry all the state variables, such as position, velocity, stress, strain, etc. Besides, an Eulerian background grid is used to integrate the momentum equations and to calculate space derivatives^[11,12]. In each time step, the particles are rigidly attached to the Eulerian background grid and move with it. Firstly, the kinematic variables are mapped from particles to grid nodes to establish grid nodal momentum equations. And then, the solutions of the grid nodal momentum equations are mapped from the grid nodes back to the particles to update their positions and velocities. The deformed background grid is discarded at the end of each time step, and a new regular background grid is employed for the next time step. Therefore, the mesh distortion caused by extreme deformation is avoided, and numerical difficulties associated with the Eulerian method are overcome. Moreover, the MPM shows advantages of computational efficiency and stability over the SPH method^[13]. So far, the MPM and its extensions have been widely applied to many problems involving extreme material deformation^[14], such as explosion and impact^[15], geomechanics^[16], cracking expansion^[17], and multiphase flows^[18], just to name a few. However, the efficiency of the MPM is lower than that of the FEM due to the mapping between the background grid and particles, and the accuracy of particle quadrature used in the MPM is lower than that of Gauss quadrature used in the FEM^[11,14]. Hence, Zhang and his group developed several coupling schemes to take full advantages of both MPM and FEM, such as the explicit material point finite element method (MPFEM)^[19], hybrid finite element material point method (HFEMP)^[20], the coupled finite element material point method (CFEMP)^[21,12] and the adaptive finite element material point method (AFEMP)^[11].

In this paper, a coupled shell-material point method is developed for bird strike simulations to take full advantages of both FEM and MPM. During a bird strike, the bird undergoes large deformation like flows over the structures, while most part of the aircraft is in small deformation. Thus, the bird is discretized by MPM particles, while the thin-walled structures in the aircraft are discretized by shell elements. The MPM particles are coupled with shell elements based on a particle-to-surface contact algorithm^[22] to model the interaction between the bird and the aircraft. The structures near the impact point may experience large deformations, even fail, which may decrease the computational accuracy and the time step size. To avoid these difficulties, the distorted and failed shell elements will be eroded if a certain criterion is reached.

The remaining parts of the paper is organized as follows. Section 2 and Section 3 briefly describe the MPM and Belytschko-Lin-Tsay shell element formulation, respectively. The coupling scheme of the MPM particles with shell elements is developed in Section 4. Section 5 summarizes the numerical algorithm of the CSMPM, and Section 6 presents several numerical examples to validate the developed method. Finally, conclusions are drawn in Section 7.

2. Brief review of MPM

As depicted in Figure 1, the material domain Ω is discretized by a set of particles, which carry all the state variables. Due to the mass lumped at each particle, density is approximated by the Dirac delta function δ as

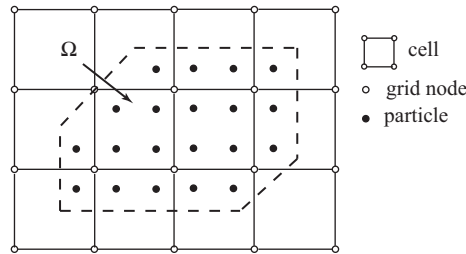


Figure 1: MPM discretization

$$\rho(\mathbf{x}) = \sum_{p=1}^{n_p} M_p \delta(\mathbf{x} - \mathbf{x}_p) \quad (1)$$

where the subscript p indicates the variable carried by particle p , n_p is the total number of particles, and M_p and \mathbf{x}_p are the mass and coordinate of particle p . The momentum equation for the material domain is given as

$$\sigma_{ji,j} + \rho b_i = \rho \ddot{u}_i \quad (2)$$

where the subscripts i and j denote the components of the space with Einstein summation convention, the superimposed dot indicates time derivatives, σ_{ij} is the Cauchy stress, b_i is the body force per unit mass, ρ is the current density, and u_i is the displacement. Taking the virtual displacement δu_i as the test function, the weak form of the momentum equation of Eq.(2) with zero prescribed traction boundary can be written as

$$\int_{\Omega} \rho \ddot{u}_i \delta u_i d\Omega + \int_{\Omega} \sigma_{ij} \delta u_{i,j} d\Omega - \int_{\Omega} \rho b_i \delta u_i d\Omega = 0 \quad (3)$$

In each time step, the particles are rigidly attached to the background grid, and the displacement u_{ip} of the particle p can be obtained by interpolating the grid nodal displacement u_{iI} as

$$u_{ip} = \sum_{I=1}^{n_g} N_{Ip} u_{iI} \quad (4)$$

where the subscript I denotes the variables associated with grid node I , n_g is the number of nodes defining the cell that contains material point p , and $N_{Ip} = N_I(\xi_p, \eta_p, \zeta_p)$. For 3D problems, the 8-point hexahedral cell is usually employed, so that the tri-linear shape function is applied as follows

$$N_I(\xi, \eta, \zeta) = \frac{1}{8} (1 + \xi_I \xi) (1 + \eta_I \eta) (1 + \zeta_I \zeta) \quad I = 1, 2, \dots, 8 \quad (5)$$

where $\xi \in [-1, 1]$, $\eta \in [-1, 1]$ and $\zeta \in [-1, 1]$ are the nature coordinates, and ξ_I, η_I and ζ_I take their nodal values of $(\pm 1, \pm 1, \pm 1)$.

Substituting Eqs.(1) and (4) into Eq.(3) and invoking the arbitrariness of δu_{iI} leads to

$$\dot{p}_{iI} = f_{iI}^{\text{ext}} - f_{iI}^{\text{int}} \quad I = 1, 2, \dots, n_g \quad (6)$$

where

$$p_{iI} = M_I v_{iI} \quad (7)$$

is the nodal momentum of grid point I ,

$$f_{iI}^{\text{int}} = \sum_{p=1}^{n_p} N_{Ip,j} \sigma_{ijp} \frac{M_p}{\rho_p} \quad (8)$$

is the internal force,

$$f_{iI}^{\text{ext}} = \sum_{p=1}^{n_p} M_p N_{Ip} b_{ip} \quad (9)$$

is the external force, and $\sigma_{ijp} = \sigma_{ij}(\mathbf{x}_p)$, $b_{ip} = b_i(\mathbf{x}_p)$.

In Eq.(7), the lumped mass matrix is used, namely

$$M_I = \sum_{p=1}^{n_p} N_{Ip} M_p \quad (10)$$

The leap-frog central difference time integration algorithm is used to integrate the momentum equation of Eq.(6). In the following equations, the superscript k denotes the value of variable at time t^k . Given u_{ip}^k and $\dot{u}_{ip}^{k-1/2}$, we seek for the solution at time t^{k+1} . From Eq.(6) and Fig.2, the grid nodal momentum can be updated by

$$p_{iI}^{k+\frac{1}{2}} = p_{iI}^{k-\frac{1}{2}} + (f_{iI}^{\text{ext},k} - f_{iI}^{\text{int},k}) \Delta t^k \quad (11)$$

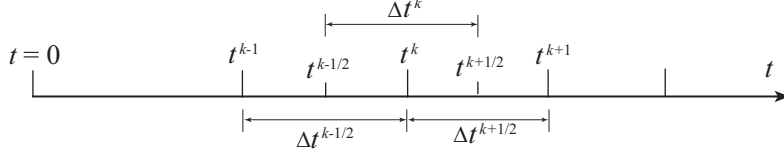


Figure 2: Time intervals

Then the position x_{ip}^{k+1} and velocity $v_{ip}^{k+1/2}$ of particle p are updated by

$$x_{ip}^{k+1} = x_{ip}^k + \Delta t^{k+1/2} \sum_{I=1}^{n_g} v_{iI}^{k+1/2} N_{Ip}^k \quad (12)$$

$$v_{ip}^{k+1/2} = v_{ip}^{k-1/2} + \Delta t^k \sum_{I=1}^{n_g} a_{iI}^k N_{Ip}^k \quad (13)$$

where $v_{iI}^{k+1/2} = p_{iI}^{k+1/2}/M_I^k$, $a_{iI}^k = f_{iI}^k/M_I^k$ and $f_{iI}^k = f_{iI}^{\text{ext},k} - f_{iI}^{\text{int},k}$. As shown in Figure 2, the time intervals are defined as

$$\Delta t^k = \frac{\Delta t^{k-\frac{1}{2}} + \Delta t^{k+\frac{1}{2}}}{2}, \quad \Delta t^{k-\frac{1}{2}} = t^k - t^{k-1}, \quad \Delta t^{k+\frac{1}{2}} = t^{k+1} - t^k \quad (14)$$

The critical time step size is determined by

$$\Delta t_{\text{cr}} = \frac{d_c}{\max_p (c_p + |v_p|)} \quad (15)$$

where d_c is the cell spacing, c_p and v_p are the material local sound speed and velocity of particle p . The cell spacing d_c is constant in the MPM because the same regular background grid cell is usually used in all time steps.

After that, all the variables assigned to the grid nodes are reset to zero, which indicates that a new regular background grid is used in the next time step.

3. Belytschko-Lin-Tsay shell element

The Belytschko-Lin-Tsay shell element^[23], which is based on a corotational velocity-strain formulation, is employed in this paper to model the aircraft. It shows significant speed advantage over other shell elements in crash and impact simulations, and has been used in LS-DYNA^[24], PAMCRASH^[25] and ABAQUS^[26].

The geometry of the shell is defined by its reference surface, which is usually the mid-surface of the shell and determined by the nodal coordinates of the elements. The element corotational system $(\hat{x}, \hat{y}, \hat{z})$ is embedded in and deforms with the element. The unit vectors $(\mathbf{e}_1, \mathbf{e}_2, \mathbf{e}_3)$ corresponding to this local coordinate system are constructed, as shown in Fig.3^[27]. The midpoints of the sides are connected by lines, \mathbf{r}_{ac} and \mathbf{r}_{bd} , then the unit vector \mathbf{e}_3 is obtained by

$$\mathbf{e}_3 = \frac{\mathbf{r}_{\text{ac}} \times \mathbf{r}_{\text{bd}}}{\|\mathbf{r}_{\text{ac}} \times \mathbf{r}_{\text{bd}}\|}, \quad (16)$$

where \times denotes the vector cross product and $\|\bullet\|$ indicates the norm of a vector. Then the other two unit vectors are defined by

$$\mathbf{e}_1 = \frac{\mathbf{r}_{\text{ac}}}{\|\mathbf{r}_{\text{ac}}\|}, \quad (17)$$

$$\mathbf{e}_2 = \mathbf{e}_3 \times \mathbf{e}_1. \quad (18)$$

The transformation matrix \mathbf{q} between the global and local element coordinate systems is defined by the corotational triad $(\mathbf{e}_1, \mathbf{e}_2, \mathbf{e}_3)$ as

$$\mathbf{q} = \begin{bmatrix} e_{1x} & e_{2x} & e_{3x} \\ e_{1y} & e_{2y} & e_{3y} \\ e_{1z} & e_{2z} & e_{3z} \end{bmatrix}, \quad (19)$$

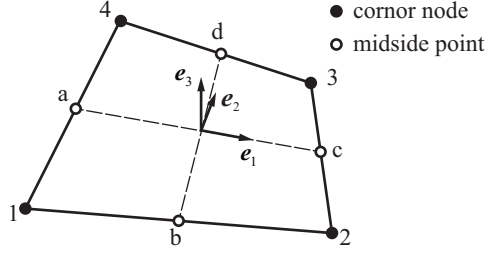


Figure 3: Corotational coordinate system

where e_{ix}, e_{iy}, e_{iz} are the global components of the element coordinate unit vector \mathbf{e}_i . The transformation from element coordinate components $\hat{\mathbf{r}}$ to global coordinate components \mathbf{r} is defined as

$$\mathbf{r} = \mathbf{q}\hat{\mathbf{r}}, \quad (20)$$

and the inverse transformation is defined by the matrix transpose, i.e.,

$$\hat{\mathbf{r}} = \mathbf{q}^T \mathbf{r}. \quad (21)$$

The element employs the Mindlin^[28] theory of plates and shells to partition the velocity of any point in the shell as

$$\hat{\mathbf{v}} = \hat{\mathbf{v}}^m - \hat{z}\mathbf{e}_3 \times \hat{\boldsymbol{\omega}}, \quad (22)$$

where \mathbf{v}^m is the velocity of the reference surface, $\boldsymbol{\omega}$ is the angular velocity vector, and \hat{z} is the distance to the reference surface along the normal direction of the shell element.

The corotational components of the velocity strain (rate of deformation) are given by

$$\hat{d}_{ij} = \frac{1}{2} \left(\frac{\partial \hat{v}_i}{\partial \hat{x}_j} + \frac{\partial \hat{v}_j}{\partial \hat{x}_i} \right). \quad (23)$$

Substituting Eq.(22) into Eq.(23) gives

$$\begin{aligned} \hat{d}_x &= \frac{\partial \hat{v}_x^m}{\partial \hat{x}} + \hat{z} \frac{\partial \hat{\omega}_y}{\partial \hat{x}}, & \hat{d}_y &= \frac{\partial \hat{v}_y^m}{\partial \hat{y}} - \hat{z} \frac{\partial \hat{\omega}_x}{\partial \hat{y}}, \\ 2\hat{d}_{xy} &= \frac{\partial \hat{v}_x^m}{\partial \hat{y}} + \frac{\partial \hat{v}_y^m}{\partial \hat{x}} + \hat{z} \left(\frac{\partial \hat{\omega}_y}{\partial \hat{y}} - \frac{\partial \hat{\omega}_x}{\partial \hat{x}} \right), \\ 2\hat{d}_{yz} &= \frac{\partial \hat{v}_z^m}{\partial \hat{y}} - \hat{\omega}_x, & 2\hat{d}_{xz} &= \frac{\partial \hat{v}_z^m}{\partial \hat{x}} + \hat{\omega}_y. \end{aligned} \quad (24)$$

The velocity strain \hat{d}_z is computed from the plane stress assumption of

$$\hat{\sigma}_z = 0, \quad (25)$$

where $\hat{\sigma}$ is the physical Cauchy stress, which is work-conjugate to the above strain rate and can be updated by a constitutive model.

The standard bilinear isoparametric shape functions are used to interpolate the translate velocity, the angular velocity, and the element's coordinates on the reference surface, namely

$$\begin{aligned} \mathbf{v}^m &= N_I(\xi, \eta) \mathbf{v}_I, \\ \boldsymbol{\omega} &= N_I(\xi, \eta) \boldsymbol{\omega}_I, \\ \mathbf{x}^m &= N_I(\xi, \eta) \mathbf{x}_I, \end{aligned} \quad (26)$$

where

$$N_I(\xi, \eta) = \frac{1}{2} (1 + \xi_I \xi) (1 + \eta_I \eta), \quad (27)$$

and the subscript I denotes variables associated with node I . The standard summation convention is used for repeated superscripts and subscripts.

Substituting Eq.(26) into Eq.(24) gives

$$\begin{aligned} \hat{d}_x &= B_{1I} \hat{v}_{xI} + \hat{z} B_{1I} \hat{\omega}_{yI}, & \hat{d}_y &= B_{2I} \hat{v}_{yI} - \hat{z} B_{2I} \hat{\omega}_{xI} \\ 2\hat{d}_{xy} &= B_{2I} \hat{v}_{xI} + B_{1I} \hat{v}_{yI} + \hat{z} (B_{2I} \hat{\omega}_{yI} - B_{1I} \hat{\omega}_{xI}), \\ 2\hat{d}_{yz} &= B_{2I} \hat{v}_{zI} - N_I \hat{\omega}_{xI}, & 2\hat{d}_{xz} &= B_{1I} \hat{v}_{zI} + N_I \hat{\omega}_{yI}. \end{aligned} \quad (28)$$

where

$$B_{1I} = \frac{\partial N_I}{\partial \hat{x}}, \quad B_{2I} = \frac{\partial N_I}{\partial \hat{y}}, \quad (29)$$

By using the one-point quadrature, Eq.(29) at the center of the element, i.e., at $\xi = \eta = 0$, can be calculated by

$$\begin{Bmatrix} B_{1I} \\ B_{2I} \end{Bmatrix} = \frac{1}{2A} \begin{bmatrix} \hat{y}_2 - \hat{y}_4 & \hat{y}_3 - \hat{y}_1 & \hat{y}_4 - \hat{y}_2 & \hat{y}_1 - \hat{y}_3 \\ \hat{x}_4 - \hat{x}_2 & \hat{x}_1 - \hat{x}_3 & \hat{x}_2 - \hat{x}_4 & \hat{x}_3 - \hat{x}_1 \end{bmatrix} \quad (30)$$

and A is the area of the element.

After the Cauchy stresses are updated by a constitutive model, the local nodal forces and moments can be obtained by the principle of virtual work as

$$\begin{aligned} \hat{f}_{xI} &= A (B_{1I} f_{xx}^e + B_{2I} f_{xy}^e), \\ \hat{f}_{yI} &= A (B_{2I} f_{yy}^e + B_{1I} f_{xy}^e), \\ \hat{f}_{zI} &= \kappa A (B_{1I} f_{xz}^e + B_{2I} f_{yz}^e), \\ \hat{m}_{xI} &= A (B_{2I} m_{yy}^e + B_{1I} m_{xy}^e - \frac{1}{4} \kappa f_{yz}^e), \\ \hat{m}_{yI} &= A (-B_{1I} m_{xx}^e - B_{2I} m_{xy}^e + \frac{1}{4} \kappa f_{xz}^e), \\ \hat{m}_{zI} &= 0, \end{aligned} \quad (31)$$

where

$$f_{\alpha\beta}^e = \int_h \hat{\sigma}_{\alpha\beta} d\hat{z}, \quad m_{\alpha\beta}^e = - \int_h \hat{z} \hat{\sigma}_{\alpha\beta} d\hat{z}, \quad (32)$$

and κ is the shear factor of the Mindlin theory, which is usually taken to be $\frac{5}{6}$. Then the local forces and moments are transformed to the global coordinate system using the transformation relation given previously as Eq.(20).

Since the one-point quadrature is used, the hourglass modes are possible for this element. The hourglass control scheme proposed by Flanagan and Belytschko^[29] is used here, and its details will not be repeated here for simplicity.

The translational momentum equation for the shell element node is quite similar to Eq.(2), while the rotational one can be given as

$$R_I \dot{\omega}_{iI} = m_{iI} \quad (33)$$

where R_I is the rotational mass of node I . The leap-frog central difference time integration algorithm is used to integrate the momentum equations. The translate and angular velocities, and positions of node I can be updated by

$$v_{iI}^{k+\frac{1}{2}} = v_{iI}^{k-\frac{1}{2}} + \frac{f_{iI}^k}{M_I} \quad (34)$$

$$\omega_{iI}^{k+\frac{1}{2}} = \omega_{iI}^{k-\frac{1}{2}} + \frac{m_{iI}^k}{R_I} \quad (35)$$

$$x_{iI}^{k+1} = x_{iI}^k + \Delta t^{k+\frac{1}{2}} v_{iI}^{k+\frac{1}{2}} \quad (36)$$

The critical time step size is determined by

$$\Delta t = \min(L_e/c) \quad (37)$$

where L_e is the characteristic length of element e , and c is the material local sound speed. In order to keep all operations synchronic in the same loop, the minimum critical time step size of the FEM and MPM domains is used as the time step size.

Under the high-velocity impact from the bird, the structures may undergo large deformation and even fail. The FEM mesh may distort, which will decrease the numerical accuracy and efficiency dramatically. The simplest way to deal with the problem is to introduce an erosion scheme of the distorted shell elements. For instance, if a shell element's equivalent plastic strain or its degree of element distortion exceeds a user-specified value, the erosion will be activated, and then the Gauss integration for this shell element will be neglected, which has been widely used in many codes including LS-DYNA.

4. Coupling scheme

The coupling of MPM particles with shell elements is implemented by a particle-to-surface contact algorithm^[22]. Each shell element has two faces, called segments, which are offset from its reference surface with one half of the element's thickness. The particle-to-surface contact algorithm is composed of three steps: a global search step to find the potential contact pairs (a particle and a shell element), a local search step to calculate the exact contact position and the gap between the contact pairs, and the contact force imposed between the contact pair to prevent the penetration.

The global search uses the bucket-sorting scheme^[30] to minimize the computational costs. As shown in Fig.4, a uniform bucket cell structure is set to overlay all the contact bodies. The key part of this searching procedure is to identify the cell number for each particle and segment. Then the segment and the MPM particles, which locate in the same bucket cell, are considered as potential contact pairs. In consideration of the thickness of shell and robustness of the scheme, a slightly larger range of the bucket cells is searched for each shell element. Besides, the bucket cell size is taken to be close to the average segment size for higher efficiency, as recommended by Belytschko and Lin^[30].

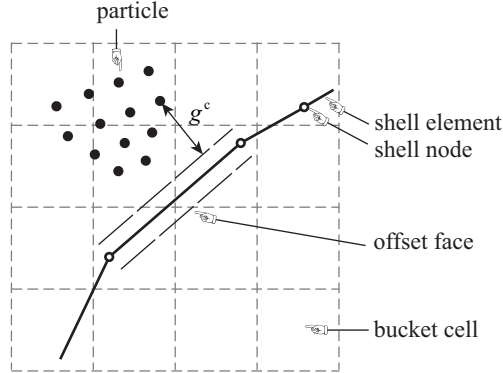


Figure 4: Bucket-sorting

The local search determines the exact contact position and the gap between the contact pairs. Assume that the contact point of particle P on the element's reference surface is point C , as shown in Fig.5, whose coordinates can be obtained by interpolating the element's nodal coordinates using Eq.(26). The two tangent vectors of the surface at point C can be obtained by

$$\mathbf{t}^\xi = \frac{\partial \mathbf{x}}{\partial \xi}, \quad \mathbf{t}^\eta = \frac{\partial \mathbf{x}}{\partial \eta}. \quad (38)$$

where \mathbf{x} denotes the position vector of point C .

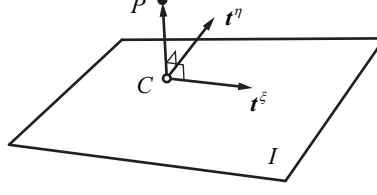


Figure 5: Local search

The vector from the contact point C to particle P should be perpendicular to the reference surface, so that the local coordinates (ξ_C, η_C) of the contact point C can be obtained by solving

$$\begin{aligned} \frac{\partial \mathbf{x}}{\partial \xi}(\xi_C, \eta_C) \cdot [\mathbf{x}_P - \mathbf{x}(\xi_C, \eta_C)] &= 0 \\ \frac{\partial \mathbf{x}}{\partial \eta}(\xi_C, \eta_C) \cdot [\mathbf{x}_P - \mathbf{x}(\xi_C, \eta_C)] &= 0 \end{aligned} \quad (39)$$

which are binary cubic nonlinear equations and can be solved by the Newton-Raphson iterative method. The gap of this contact pair can be calculated by

$$g^c = \mathbf{n}_C \cdot [\mathbf{x}_P - \mathbf{x}(\xi_C, \eta_C)] - \frac{h}{2} \quad (40)$$

where h is the thickness of the element and

$$\mathbf{n}_C = \frac{\mathbf{t}^\xi \times \mathbf{t}^\eta}{\|\mathbf{t}^\xi \times \mathbf{t}^\eta\|}(\xi_C, \eta_C) \quad (41)$$

is the unit normal vector of the surface pointing outwards at the contact point C .

If penetration appears, i.e., $g^c < 0$, an appropriate contact force should be imposed between the contact pair to prevent the penetration. The normal contact force can be determined by the penalty method^[24] or the Lagrangian multiplier method^[22]. The penalty contact force imposed on particle P can be expressed as

$$\mathbf{f}_P^{c, \text{pen}} = -s^{\text{pen}} K^c g^c \mathbf{n}_C \quad (42)$$

where s^{pen} is a user-defined scale factor for contact stiffness, and K^c is the contact stiffness, which can be calculated by^[24]

$$K^c = \begin{cases} \frac{KA^2}{V} & \text{for solid element} \\ \frac{KA}{D_{\max}} & \text{for shell element} \end{cases} \quad (43)$$

where A , D_{\max} , K and V are the segment's area, maximum of diagonals, bulk modulus and volume of the element that contains the segment, respectively. The contact force of the Lagrangian multiplier method can be expressed as^[22]

$$\mathbf{f}_P^{c, \text{lag}} = \frac{M_P M_C (\mathbf{v}_C - \mathbf{v}_P)}{(M_P + M_C) \Delta t} \quad (44)$$

where M_P and \mathbf{v}_P are the mass and velocity of particle P , \mathbf{v}_C is the interpolated velocity of the contact point C , and M_C denotes the equivalent mass of the contact point, which can be calculated by^[22]

$$M_C = \frac{1}{\sum_{I=1}^{n_I} \frac{N_I^2(\xi_C, \eta_C)}{M_I}} \quad (45)$$

where n_I is the total number of nodes of the segment, and the summation convention is not used for subscript I here.

As the explicit momentum equations are solved at the grid node in the MPM domain, the contact force of particle P is transformed to grid node I by the shape function as

$$\mathbf{f}_I^c = N_I^{\text{MPM}}(\xi_P, \eta_P) \mathbf{f}_P^c \quad (46)$$

Similarly, the contact force of point C in the finite element domain is transformed to element node I as

$$\mathbf{f}_I^c = N_I^{\text{FEM}}(\xi_C, \eta_C) \mathbf{f}_C^c \quad (47)$$

where $\mathbf{f}_C^c = -\mathbf{f}_P^c$.

5. Computer Implementation

The proposed ASMPM has been implemented in our three-dimensional explicit MPM code, MPM3D^[31,32]. The Numerical algorithm for one time step can be summarized as follows:

1. Redefine the background grid, map the masses and momenta of all the particles to the background grid nodes by

$$M_I^k = \sum_{p=1}^{n_p} N_{Ip}^k M_p \quad (48)$$

$$p_{iI}^{k-\frac{1}{2}} = \sum_{p=1}^{n_p} N_{Ip}^k M_p v_{ip}^{k-\frac{1}{2}} \quad (49)$$

where N_{Ip}^k is the shape function of grid point I evaluated at material point p at the k th time step.

2. Apply the essential boundary conditions on the background grid nodes. If node I is fixed in the i direction, set $p_{iI}^{k-\frac{1}{2}} = 0$.
3. For the MPM body, loop over all the particles to calculate their rate of deformations

$$D_{ijp}^{k-\frac{1}{2}} = \frac{1}{2} \sum_{I=1}^8 \left[N_{Ip,j}^k v_{iI}^{k-\frac{1}{2}} + N_{Ip,i}^k v_{jI}^{k-\frac{1}{2}} \right] \quad (50)$$

spin tensors

$$\Omega_{ijp}^{k-\frac{1}{2}} = \frac{1}{2} \sum_{I=1}^8 \left[N_{Ip,j}^k v_{iI}^{k-\frac{1}{2}} - N_{Ip,i}^k v_{jI}^{k-\frac{1}{2}} \right] \quad (51)$$

densities

$$\rho_p^{k+1} = \frac{\rho_p^k}{1 + \Delta \varepsilon_{iip}^{k-\frac{1}{2}}} \quad (52)$$

and then update the Cauchy stress σ_{ijp}^k using the corresponding constitutive model and equation of state. In the above equations, $v_{iI}^{k-\frac{1}{2}} = p_{iI}^{k-\frac{1}{2}}/M_I^k$ is the velocity of grid node I , and $\Delta \varepsilon_{ijp}^{k-\frac{1}{2}} = \Delta t^k D_{ijp}^{k-\frac{1}{2}}$ is the incremental strain. Finally, the MPM grid nodal internal forces $f_{iI}^{\text{int},k}$ and external force $f_{iI}^{\text{ext},k}$ are calculated by using Eqs.(8) and (9), respectively.

4. For shell elements, calculate the nodal force and moment as described in Section 3.
5. Assume that the MPM particles are not in contact with any shell elements, calculate the trial momenta $p_{iI}^{k+\frac{1}{2},\text{trial}}$ of the MPM grid nodes and the FEM nodes using Eq.(11) , and then calculate the trial velocities of the particles and the FEM nodes.
6. Calculate the contact force $f_{iI}^{c,k}$ of the MPM grid nodes and the FEM nodes with the trial velocity, as described in Section 4.
7. Update the momenta and force of the MPM grid nodes and the FEM nodes by

$$p_{iI}^{k+\frac{1}{2}} = p_{iI}^{k+\frac{1}{2},\text{trial}} + \Delta t^k f_{iI}^{c,k} \quad (53)$$

$$f_{iI}^k = f_{iI}^{\text{ext},k} - f_{iI}^{\text{int},k} + f_{iI}^{c,k} \quad (54)$$

8. Update the velocities $v_{ip}^{k+\frac{1}{2}}$ and positions x_{ip}^{k+1} of all the MPM particles by Eqs.(13) and (12). Update the translate velocities $v_{iI}^{k+\frac{1}{2}}$, the angular velocities $\omega_{iI}^{k+\frac{1}{2}}$, and positions x_{iI}^{k+1} of all the FE nodes by Eqs.(34), (35) and (36), respectively.
9. All distorted shell elements will be eroded according to a certain criterion.
10. Discard the deformed background grid for MPM and go to step 1 to start a new time step.

6. Numerical Simulations

To validate the method, the bird impacts on a rigid plate, an aluminum plate, and a wing leading edge are simulated in this section. As suggested by many studies^[1,5,8,33,34], the substitute bird is approximated as a hemispherical-ended cylinder with a length-to-diameter ratio of two, as shown in Fig.6(a), and the bird has a density of 950 kg/m^3 and a porosity of 10%. In accordance with certification requirements, the bird's mass usually takes 1.82 kg (4 lb) or 3.64 kg (8 lb)^[1], from which the diameter D in Fig.6(a) is determined to be 114mm or 143mm, respectively. Then the bird is discretized by evenly distributed particles, as shown in Fig.6(b).

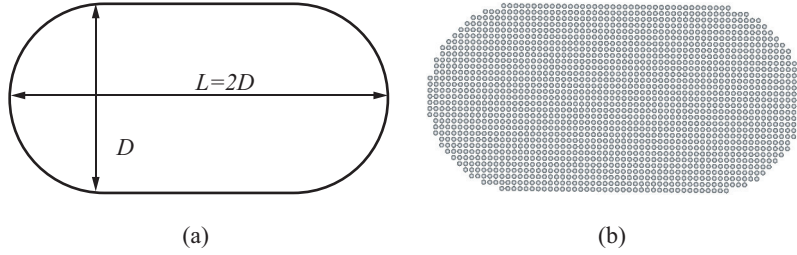


Figure 6: Bird model geometry (a) and particle discretization (b)

At the velocities of interest, the bird does not have enough shear strength against the generated high pressures and behaves as a homogenous jet of fluid^[3,5]. Hence, a null material model with an equation of state (EOS) is usually adopted to represent the behavior of the bird. In this paper, the cubic polynomial EOS is used, which relates the pressure and volume by

$$P = C_0 + C_1\mu + C_2\mu^2 + C_3\mu^3 + (C_4 + C_5\mu + C_6\mu^2) E \quad (55)$$

where P is the pressure, $\mu = \rho/\rho_0 - 1$, ρ and ρ_0 are the current and initial densities of the material, respectively; E is the internal energy per volume, and parameters C_0 to C_6 are material constants. The null material model relates the stress and strain by

$$\sigma_{ij} = -P\delta_{ij} + 2\nu_d\dot{D}_{ij} \quad (56)$$

where δ_{ij} and \dot{D}_{ij} are the identity and the rate-of-deformation tensors, respectively, and ν_d is the dynamic viscosity.

Referring to many studies^[35–37], we chose these parameters as: $C_0 = C_2 = \dots = C_6 = 0$, $C_1 = 2250 \text{ MPa}$ and $\nu_d = 0 \text{ Pa}\cdot\text{s}$.

In the third bird strike simulation, if any quadrature point's equivalent plastic strain exceeds $\varepsilon_f = 0.2$, the parent shell element will be eroded.

6.1. Bird impact on a rigid plate

As a benchmark calculation, a 1.0 kg bird impacts onto a $500 \text{ mm} \times 500 \text{ mm}$ square steel plate perpendicularly. Given the geometry of Fig.6(a) and a density of 950 kg/m^3 , the bird has a diameter of 93 mm and a length of 186 mm, and is discretized by 38734 evenly distributed particles with a spacing of 3 mm. The plate has a thickness of 15 mm, which is large enough to be considered as rigid, and is meshed by 25×25 shell elements with dimension of 20 mm. The plate is modelled by an elastic material model with density $\rho = 7800 \text{ kg/m}^3$, elastic modulus $E = 200 \text{ GPa}$ and Poisson's ratio $\nu = 0.3$. We don't use the rigid model because in our penalty contact algorithm the penalty parameter is decided by Young's modulus of the plate.

All the nodes of the plate are fixed, and the initial velocity of the bird is set as 116 m/s. The total simulation time is 1.6 ms. For comparison, we build a similar model in LS-DYNA, which simply replaces the MPM bird with a SPH bird and uses the soft constraint penalty contact formulation.

Fig.7 shows the typical phases of the impact. The red particles are MPM particles and the gray particles are SPH particles. As can be seen, both our MPM bird and the DYNA's SPH bird behave like fluid, and the configurations at all times match well. However, the SPH bird seems to be scattered, which may be a result

of the tensile instability, while the MPM bird doesn't suffer such issue. In the tensile instability, the particles clump together and large voids are formed. The instability results from an effective stress with a negative modulus (imaginary sound speed) being produced by the interaction between the constitutive relation and the kernel function^[38].

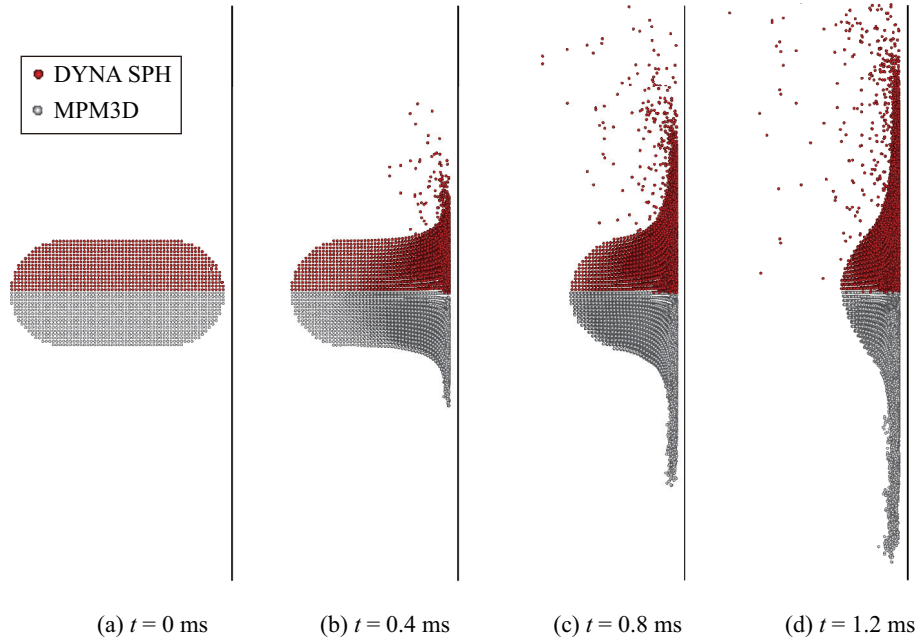


Figure 7: Configurations of the bird at different times. The red particles are MPM particles and the gray particles are SPH particles

Fig.8 compares the time history of the normalized pressure at the center of the impact. The pressure is measured at the element located at the center of the plate, with the element's normal contact force divided by its area, and then normalized by the theoretical stagnation pressure (i.e., 7.1 MPa)^[8]. The time is normalized by the duration of the impact (i.e. 1.6 ms). All the four profiles are good in the sense that there is a rise of pressure at the initial impact and then the pressure stabilizes around its stagnation value. The experimental results of Wilbeck^[5,8] for the Hugoniot pressure are much lower than the numerical results. Part of the explanation of the maximums not being reached resides in the fact that the Hugoniot pressure results from a very sharp peak and the duration of the impact is very short (in the range of milliseconds). Since the data obtained depend on the response time of the transducers used to measure the pressure, it is possible that the maximums were not properly captured^[8]. According to the theoretical analysis^[5,8], the Hugoniot pressure is expected to have a maximal value of about 93.6 MPa and a stagnation pressure of 7.1 MPa, giving normalized values of 13.2 and 1.0, respectively. Although the simulated peak value is much higher than Wilbeck's test result, it agrees with the SPH's and the theoretical results reasonably. Our Lagrangian multiplier coupling scheme gives a very close Hugoniot pressure to the theoretical value. It can be concluded that the bird model used in this paper is appropriate.

The time histories of the penalty coupling scheme shows a much greater low-frequency fluctuation than the time history of other two schemes. It is hard to determine an appropriate scale factor s^{pen} in Eq.(42) when the contact pair possesses significant different material properties, which is the usual case for bird strike. After some tedious tuning work, we chose a small scale factor to obtain a relatively good result. On the contrary, the Lagrangian multiplier coupling scheme does not need additional user-defined parameters, and gives much better results than the penalty method. All the tests below will take the Lagrangian multiplier coupling scheme as default.

The radial pressure distribution at a typical steady state is plotted in Fig.9 . Wilbeck^[5,8] gave the

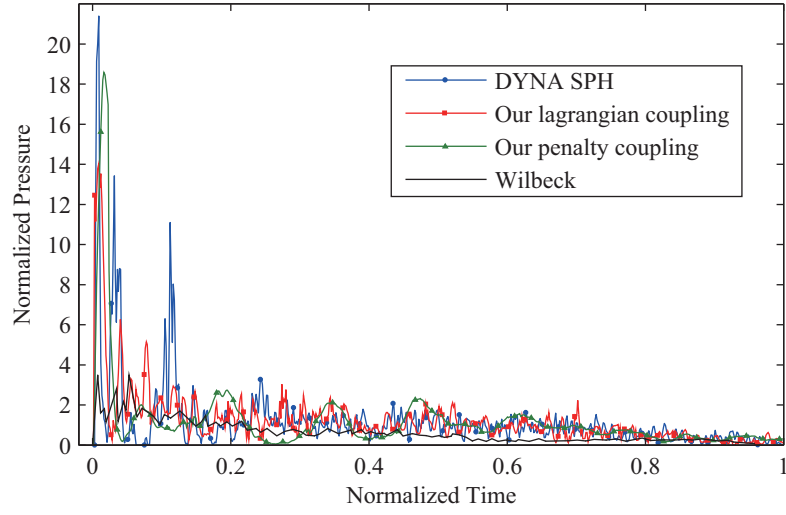


Figure 8: Time history of the normalized pressure at the center of the impact

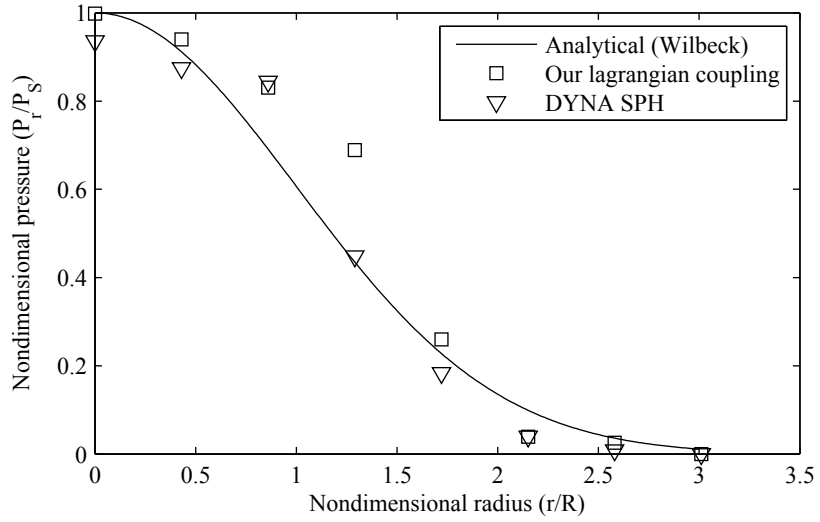


Figure 9: Radial distribution of the stagnation pressure

analytical radial pressure distribution as

$$P_r = P_S \cdot \exp \left[-\frac{1}{2} \left(\frac{r}{R} \right)^2 \right] \quad (57)$$

where r is the radial position, R is the radius of the projectile and P_S is the stagnation pressure. Since the time history of pressures obtained by the SPH method and our coupling scheme fluctuate a lot, we take the average pressure readings about the normalized time 0.5, i.e. from 7 ms to 9 ms. Fig. 9 shows that the results of our lagrangian coupling scheme and LS-DYNA agree with the analytical solution of Wilbeck reasonably.

The computational cost required by our approach and LS-DYNA are listed in Table 1. Model 1 is just the model described above. The time steps of both our approach and LS-DYNA are controlled by the shell element, and remain the same during the whole simulation. It can be seen that our approach costs only 58% of LS-DYNA. In model 2, the mesh of the plate is replaced by a coarse mesh of 1 shell element, and the time steps of both our approach and LS-DYNA are controlled by the particles of the bird. In model 3, the plate is removed, and the bird flies freely. All the results show that, our approach costs much less than LS-DYNA does.

Table 1: Comparison of computational cost

		$\Delta t_{\max}/\mu s$	$\Delta t_{\min}/\mu s$	Steps	CPU time/s
Model 1	LS-DYNA	2.40	2.40	668	161
	MPM3D	2.40	2.40	668	94
Model 2	LS-DYNA	3.17	3.03	518	125
	MPM3D	3.26	2.64	568	48
Model 3	LS-DYNA	3.17	3.17	505	107
	MPM3D	3.26	3.09	518	38

6.2. Bird impact on an aluminum plate

The square plate has a length of 500 mm, and a thickness of 14 mm. It is meshed by 2500 shell elements with the dimension of 10 mm and modelled by an isotropic elastic-plastic material model with density $\rho = 2780 \text{ kg/m}^3$, elastic modulus $E = 71 \text{ GPa}$, Poisson's ratio $\nu = 0.3$, yield strength $\sigma_Y = 345 \text{ MPa}$ and tangent modulus $E_t = 690 \text{ MPa}$. The bird weights 1.82 kg, and has a diameter of 114 mm in Fig.6(a). It is discretized by 29365 evenly distributed particles with a spacing of 4 mm. All the edges of the plate are fixed, and the initial velocity of the bird is 120 m/s. The total simulation time is 3 ms.

Fig.10 shows the configurations of the bird and the von Mises stress of the plate at different times. Both the maximum and distribution of the stress obtained by our approach are in good agreement with those of LS-DYNA. Fig.11 compares the time history of the normal displacement and equivalent plastic strain at the center of the plate. Our results agree well with those of LS-DYNA SPH approach.

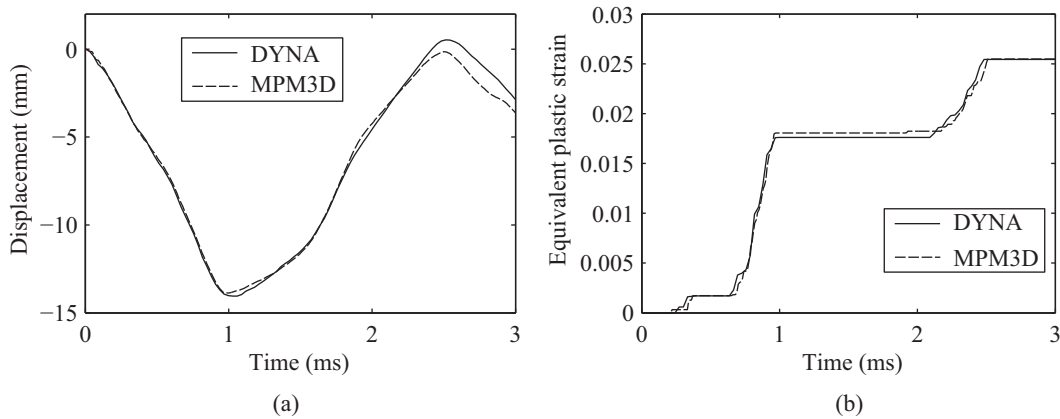


Figure 11: Deflection (a) and equivalent plastic strain (b) at the center of the plate

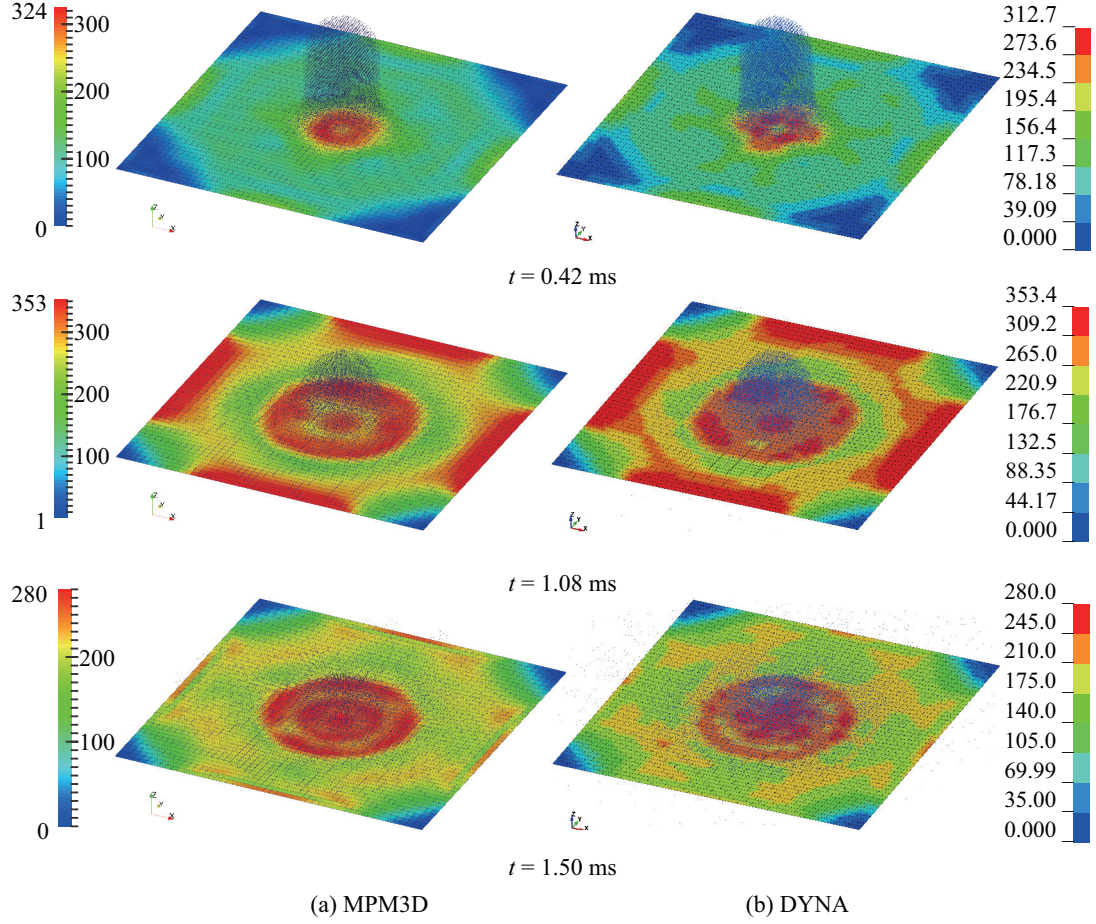


Figure 10: Configurations of the bird and von Mises stress of the plate at different times obtained by (a) MPM3D and (b) LS-DYNA

6.3. Bird strike a wing leading edge

The wing leading edge is one of the most likely place to be struck by a bird. As shown in Fig.12, the leading edge structure is composed of four ribs, one skin and one spar, which has a length of 1200 mm, a left height of 280 mm and a right height of 240 mm. The four ribs are evenly placed along the x -direction with a distance of 400 mm. As a demonstration example, all parts take a thickness of 2 mm. All parts are connected by rivets. For simplicity, only 17 rivets on one rib are plotted in Fig.12. The structure is meshed by 16309 shell elements with dimensions of about 10 mm, and modelled by an isotropic elastic-plastic material model with density $\rho = 2780 \text{ kg/m}^3$, elastic modulus $E = 71 \text{ GPa}$, Poisson's ratio $\nu = 0.3$, yield strength $\sigma_Y = 345 \text{ MPa}$ and tangent modulus $E_t = 690 \text{ MPa}$. The equivalent plastic strain beyond 0.2 is chosen as the failure criterion. Each rivet is meshed by one beam element, which has a diameter of 5 mm, tensile strength of 3000 N, and shear strength of 4800 N. All the nodes on the top and bottom edges of the spar and the back edges of ribs are fixed.

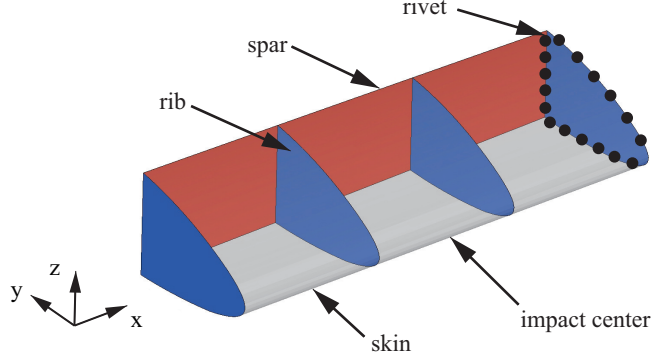


Figure 12: Wing leading edge structure

The bird is of 1.82 kg, and has a diameter of 114 mm, as shown in Fig.6(a). It is discretized by 29333 evenly distributed particles with a spacing of 4 mm. The bird impacts at the center of the structure with an initial velocity of 120 m/s along the y -direction. The total simulation time is 4 ms.

Fig.13 shows the structure's deformations and von Mises stress distributions at different times, Fig.14 shows the configuration of the bird at the final moment, and Fig.15 shows the cut shape of the structure in the end. Fig.16 shows the time history of the y -coordinate and the equivalent plastic strain of the impact center. In this example, the Lagrangian coupling scheme in MPM is used, which does not allow penetration to occur. However, the calculation of contact force by SPH is based on the penalty method, which allows slight penetration throughout the impact. Thus, the y -displacement at the impact center by MPM is slightly larger than that by LS-DYNA. In addition, the difference of contact algorithms between the ribs and the skin will also affect the final results. All the results obtained by MPM3D agree with those of LS-DYNA reasonable, which gives strong evidences to the validation and practicality of our approach.

Table 2 shows that the computational cost of our approach is slightly higher than that of LS-DYNA. Due to the intensive source code optimization, LS-DYNA costs much less than our approach does during the shell element calculation and contact calculation. On the other hand, our MPM bird costs much less than the LS-DYNA SPH bird does, as shown in Subsection 6.1. After a careful source code optimization in shell element and contact calculation, our code should be much more efficient than LS-DYNA in bird strike simulation.

Table 2: Comparison of computational cost				
	$\Delta t_{\max}/10^{-7}s$	$\Delta t_{\min}/10^{-7}s$	Steps	CPU time/s
DYNA	4.08	4.08	9807	1634
MPM3D	4.08	4.08	9801	1747

7. Conclusions

In this paper, a coupled shell-material point method is proposed for the bird strike simulation. The bird is simulated by the MPM with the cubic polynomial EOS. The shell element is highly efficient and accurate for problems with mild deformation, so it is employed to model the aircraft structure. The interaction between MPM particles and shell elements is dealt with by the particle-to-surface contact algorithm. Besides, when the structure undergoes large deformation or fails, the shell element will be eroded under a certain criterion.

As a benchmark test, a bird impact on a rigid plate is simulated, and the results show that the MPM is suitable to model the fluid-like bird. Then the example of a bird impact on an aluminum plate validates our

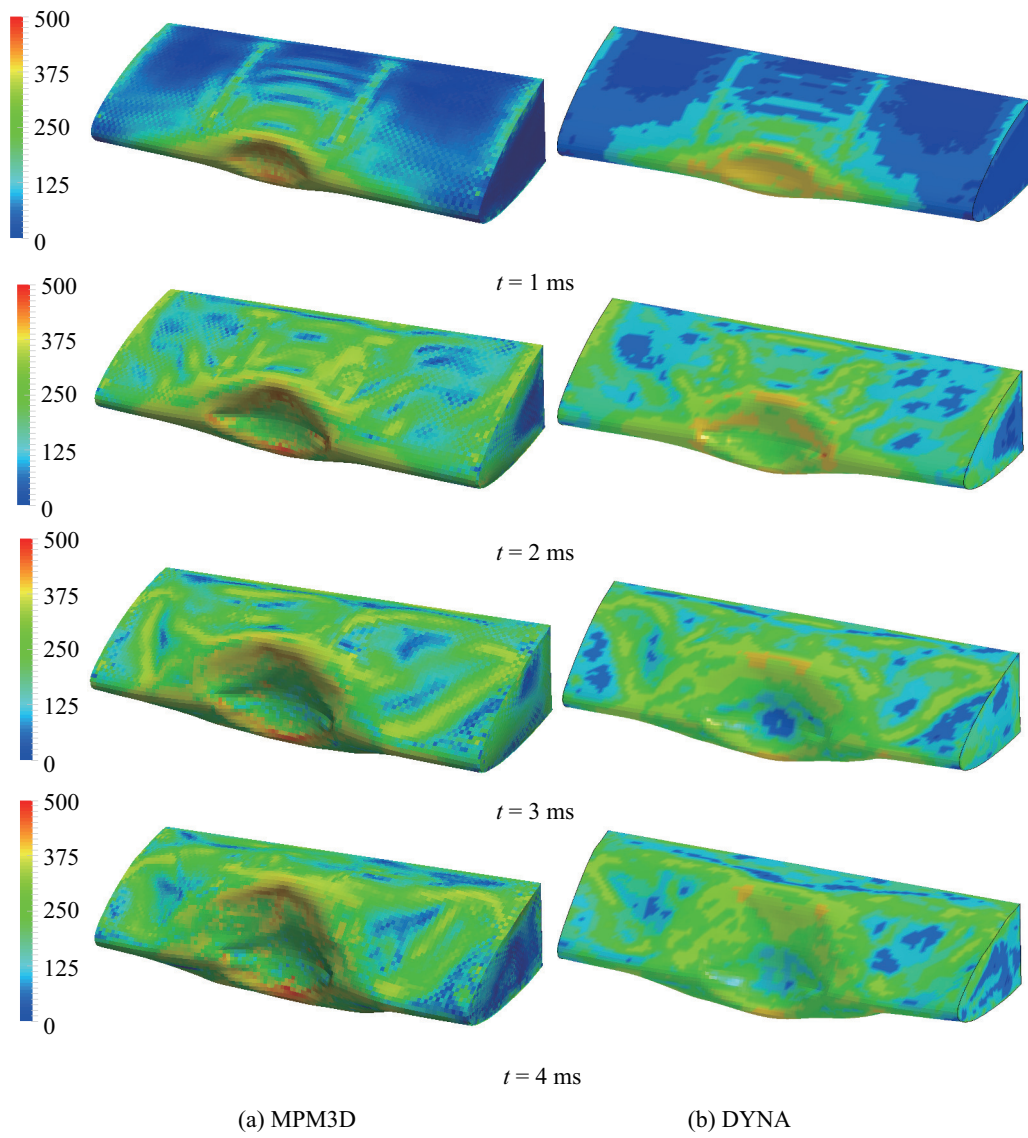


Figure 13: Deformations and von Mises stress distributions of the structure at different times

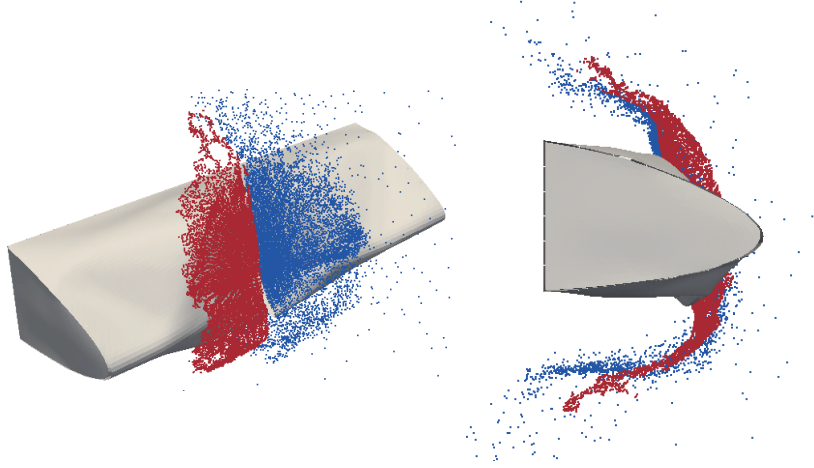


Figure 14: Configuration of the bird at the final moment. The blue particles are of SPH brid, and the red particles are of our MPM bird

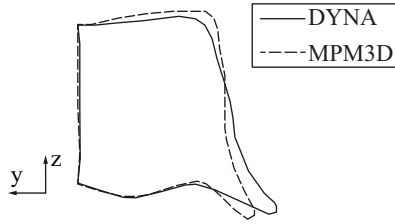


Figure 15: Cut shape of the structure at the final moment

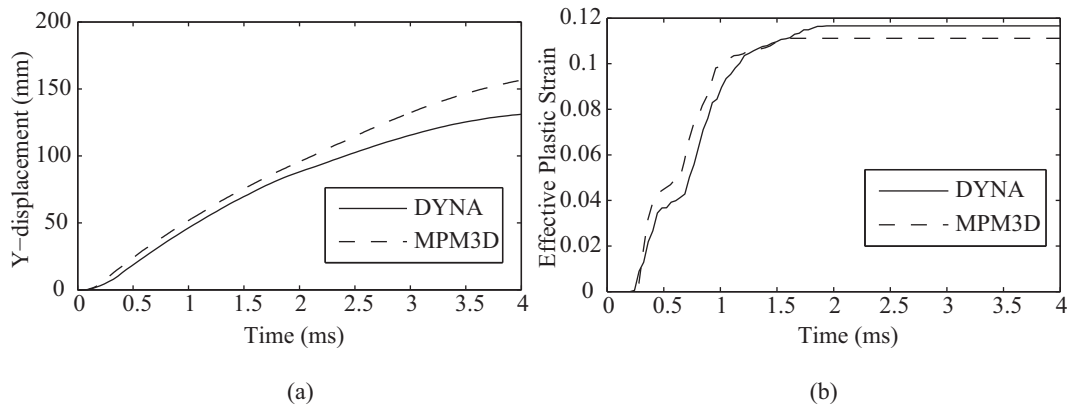


Figure 16: Time history of the y -coordinate and the equivalent plastic strain at the impact center

coupling scheme. Finally, a wing leading edge bird strike simulation is presented, and the results agree with LS-DYNA reasonably.

References

- [1] S. Heimbs, Computational methods for bird strike simulations: A review, *Computers and Structures* 89 (23-24) (2011) 2093–2112.
- [2] R. Hedayati, M. Sadighi, M. Mohammadi-aghdam, On the difference of pressure readings from the numerical , experimental and theoretical results in different bird strike studies, *Aerospace Science and Technology* 32 (1) (2014) 260–266.
- [3] R. Hedayati, M. Sadighi, *Bird Strike: An Experimental, Theoretical and Numerical Investigation*, Elsevier Science, 2015.
- [4] R. A. Dolbeer, S. E. Wright, J. R. Weller, A. L. Anderson, M. J. Begier, Wildlife strikes to civil aircraft in the united states 1990-2014, Tech. rep., FAA/USDA (2015).
- [5] J. S. Wilbeck, Impact behavior of low strength projectiles, Tech. rep., Wright-Patterson Air Force Base (1978).
- [6] S. Georgiadis, A. J. Gunnion, R. S. Thomson, B. K. Cartwright, Bird-strike simulation for certification of the boeing 787 composite moveable trailing edge, *Composite Structures* 86 (1–3) (2008) 258–268.
- [7] M. Anghileri, L.-M. L. Castelletti, V. Mazza, Birdstrike: approaches to the analysis of impacts with penetration, *Impact loading of lightweight structures* 49 (2005) 63–74.
- [8] M.-A. Lavoie, A. Gakwaya, M. Nejad Ensan, D. Zimcik, Validation of available approaches for numerical bird strike modeling tools, *Int Rev Mech Eng* 1 (4) (2007) 380–389.
- [9] D. Sulsky, Z. Chen, H. L. Schreyer, A particle method for history-dependent materials, *Computer Methods in Applied Mechanics and Engineering* 118 (1-2) (1994) 179–196.
- [10] D. Sulsky, S.-J. Zhou, H. L. Schreyer, Application of a particle-in-cell method to solid mechanics, *Computer Physics Communications* 87 (1-2) (1995) 236–252.
- [11] Y. P. Lian, X. Zhang, Y. Liu, An adaptive finite element material point method and its application in extreme deformation problems., *Computer Methods in Applied Mechanics and Engineering* 241–244 (1) (2012) 275–285.
- [12] Y. P. Lian, Y. Liu, X. Zhang, Coupling of membrane element with material point method for fluid–membrane interaction problems, *International Journal of Mechanics and Materials in Design* 10 (2) (2014) 199–211.
- [13] S. Ma, X. Zhang, X. M. Qiu, Comparison study of MPM and SPH in modeling hypervelocity impact problems, *International Journal of Impact Engineering* 36 (2009) 272–282.
- [14] Y. P. Lian, F. Zhang, Y. Liu, X. Zhang, Material point method and its applications, *Advances in Mechanics* 43 (2) (2013) 237–264.
- [15] Y. P. Lian, X. Zhang, X. Zhou, S. Ma, Y. L. Zhao, Numerical simulation of explosively driven metal by material point method, *International Journal of Impact Engineering* 38 (2011) 237–245.
- [16] S. Andersen, L. Andersen, Modelling of landslides with the material-point method, *Computational Geosciences* 14 (2010) 137–147.
- [17] J. A. Nairn, Material point method calculations with explicit cracks, *CMES-Computer Modeling in Engineering & Sciences* 4 (2003) 649–663.

- [18] D. Z. Zhang, Q. Zou, W. B. VanderHeyden, X. Ma, Material point method applied to multiphase flows, *Journal of Computational Physics* 227 (2008) 3159–3173.
- [19] X. Zhang, K. Y. Sze, S. Ma, An explicit material point finite element method for hyper velocity impact, *International Journal for Numerical Methods in Engineering* 66 (2006) 689–706.
- [20] Y. P. Lian, X. Zhang, X. Zhou, Z. T. Ma, A FEMP method and its application in modeling dynamic response of reinforced concrete subjected to impact loading, *Computer Methods in Applied Mechanics and Engineering* 200 (17-20) (2011) 1659–1670.
- [21] Y. P. Lian, X. Zhang, Y. Liu, Coupling of finite element method with material point method by local multi-mesh contact method, *Computer Methods in Applied Mechanics and Engineering* 200 (2011) 3482–3494.
- [22] Z. P. Chen, X. M. Qiu, X. Zhang, Y. P. Lian, Improved coupling of finite element method with material point method based on a particle-to-surface contact algorithm, *Computer Methods in Applied Mechanics and Engineering* 293 (2015) 1–19.
- [23] T. Belytschko, J. I. Lin, T. Chen-Shyh, Explicit algorithms for the nonlinear dynamics of shells, *Computer Methods in Applied Mechanics and Engineering* 42 (2) (1984) 225–251.
- [24] J. O. Hallquist, ANSYS/LS-DYNA Theoretical Manual, Livermore Software Technology Corporation, 2006.
- [25] ESI Group, Theory Notes Manual, PAM System International, Paris, France, 2000.
- [26] Dassault Systèmes, ABAQUS 6.12 Theory manual, Dassault Systèmes, Paris, France, 2012.
- [27] T. Belytschko, B. L. Wong, H.-Y. Chiang, Advances in one-point quadrature shell elements, *Computer Methods in Applied Mechanics and Engineering* 96 (1) (1992) 93–107.
- [28] R. D. Mindlin, Influence of rotary inertia and shear on flexural motions of isotropic, elastic plates, *Journal of Applied Mechanics* 18 (1951) 31–38.
- [29] D. P. Flanagan, T. Belytschko, A uniform strain hexahedron and quadrilateral with orthogonal hourglass control, *International Journal for Numerical Methods in Engineering* 17 (5) (1981) 679–706.
- [30] T. Belytschko, J. I. Lin, A three-dimensional impact-penetration algorithm with erosion, *Computers & structures* 25 (1) (1987) 95–104.
- [31] Z. Ma, X. Zhang, P. Huang, An object-oriented MPM framework for simulation of large deformation and contact of numerous grains, *CMES-Computer Modeling in Engineering & Sciences* 55 (1) (2010) 61–87.
- [32] X. Zhang, Y. P. Lian, Y. Liu, Z. Xu, *The Material Point Method* (in Chinese), Beijing: Tsinghua University Press, 2013.
- [33] M. A. McCarthy, J. R. Xiao, C. T. McCarthy, A. Kamoulakos, J. Ramos, J. P. Gallard, V. Melito, Modelling of bird strike on an aircraft wing leading edge made from fibre metal laminates - part 2: Modelling of impact with sph bird model, *Applied Composite Materials* 11 (5) (2004) 317–340.
- [34] R. Hedayati, S. Ziaei-Rad, Foam-core effect on the integrity of tailplane leading edge during bird-strike event, *Journal of Aircraft* 48 (6) (2011) 2080–2089.
- [35] B. Langrand, A.-S. Bayart, Y. Chauveau, E. Deletombe, Assessment of multi-physics FE methods for bird strike modelling-application to a metallic riveted airframe, *International Journal of Crashworthiness* 7 (4) (2002) 415–428.
- [36] A. G. Hanssen, Y. Girard, L. Olovsson, T. Berstad, M. Langseth, A numerical model for bird strike of aluminium foam-based sandwich panels, *International Journal of Impact Engineering* 32 (7) (2006) 1127–1144.

- [37] Q. Sun, Y. J. Liu, R. H. Jin, Numerical simulation of bird strike in aircraft leading edge structure using a new dynamic failure model, in: International Council of the Aeronautical Sciences, 2014.
- [38] J. Swegle, D. Hicks, S. Attaway, Smoothed particle hydrodynamics stability analysis, *Journal of computational physics* 116 (1) (1995) 123–134.